Magnetic and Crystal Structures of CeC2, PrC2, NdC2, TbC2, and HoC2 at Low Temperatures

M. Atoji

Citation: J. Chem. Phys. **46**, 1891 (1967); doi: 10.1063/1.1840950
View online: http://dx.doi.org/10.1063/1.1840950
View Table of Contents: http://jcp.aip.org/resource/1/JCPSA6/v46/i5
Published by the American Institute of Physics.

Magnetic and Crystal Structures of CeC_2, PrC_2, NdC_2, TbC_2, and HoC_2 at Low Temperatures*

M. Atoji
Chemistry Division, Argonne National Laboratory, Argonne, Illinois
(Received 1 November 1966)

The light rare-earth dicarbides, CeC_2, PrC_2, and NdC_2, having the tetragonal CaC_2-type structure, have been shown by neutron diffraction to become a body-centered first-kind antiferromagnet with the Néel temperatures of 33°, 15°, and 29°K and with the ordered moments being 81%, 44%, and 90% of the free-ion values, respectively. The moment direction is parallel to the c axis in the above compounds. The isostructural heavy rare-earth dicarbides, TbC_2 and HoC_2, exhibit an antiferromagnetic, elliptic-helical spin alignment propagating along the a axis with the repetition quadrupole of the atomic spacing, where the Néel temperatures are 66° and 26°K, and the root-mean-square ordered moments are 5.1 and 6.9 Bohr magnetons, respectively. Here, the moments lie on the bc plane. A modulation of the above structure takes place below 40° and 16°K, with the maximum possible additional moments of 0.54 and 1.65 Bohr magnetons at 2°K in TbC_2 and HoC_2, respectively. In TbC_2, another complex magnetic structure coexists below ~33°K. Also presented are a discussion on the wavy diffuse backgrounds of TbC_2 and HoC_2 at temperatures down to 2°K, and the low-temperature crystallographic parameters.

INTRODUCTION

THE crystal structure of the rare-earth dicarbide (REC_2) may be described as a tetragonally deformed NaCl-type packing of the RE atoms and the C_2 molecules. All of the REC_2 possess intrinsic metallic properties, in striking contrast with the isostructural alkaline-earth dicarbide which is an insulator. The neutron-diffraction studies of REC_2 (RE=La, Ce, Tb, Yb, Lu, and including Y) at room temperature have shown that[1,2]: the intramolecular C–C distance is 1.29 Å in average which is considerably longer than 1.20 Å in the alkaline-earth dicarbides[1–3]; the RE atoms excluding Yb are essentially in their tripositive Hund ground states and exhibit no significant crystal-field effect[4,5] on the paramagnetic scattering at room temperature.

Vickery *et al.*[6] have measured the magnetic susceptibilities of REC_2 (excluding RE=La, Eu, Pm, and Lu) at 450°–60°K. The susceptibilities follow the Curie–Weiss law without showing any anomaly due to the magnetic transition. Their effective magnetic moments are noticeably smaller than the RE^{3+} ground-state values (except for SmC_2) and the differences are in general larger in the lighter RE. This is apparently consistent with the usual interpretation that the crystal-field effect is larger in the light RE. However, it has been suggested[1] that these low moment values may be caused by the graphite impurity. Apart from some discrepancies between the susceptibility and neutron results, our current studies have been unveiling further details of the magnetic properties of REC_2, and in particular have established the existence of the magnetic orders in most REC_2 as described below. The statistical errors in this paper are, unless otherwise noted, expressed in terms of the standard deviation.

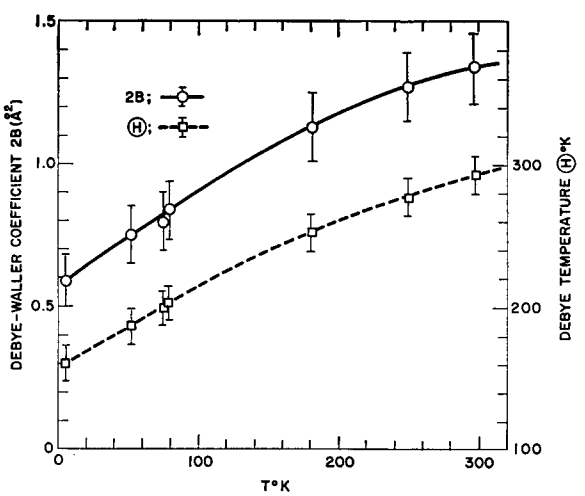

FIG. 1. The isotropic temperature-factor coefficients and the Debye characteristic temperatures of TbC_2 at low temperatures. The short vertical lines on the experimental points represent the estimated maximum errors.

CRYSTALLOGRAPHIC DATA

The samples were prepared by arc melting the stoichiometric mixture of the RE metal filings and powdered spectroscopic graphite.[7] In the impurity analysis of the products, besides examining the neutron

* Based on work performed under the auspices of the U.S. Atomic Energy Commission. A preliminary account on the subject has been reported in M. Atoji, Phys. Letters **22**, 21 (1966); **23**, 208 (1966).

[1] M. Atoji, J. Chem. Phys. **35**, 1950 (1961).
[2] M. Atoji, J. Phys. Soc. Japan Suppl. B-II **17**, 395 (1962).
[3] M. Atoji and R. C. Medrud, J. Chem. Phys. **31**, 332 (1959).
[4] G. T. Trammell, Phys. Rev. **92**, 1387 (1953).
[5] S. Odiot and D. Saint-James, J. Phys. Chem. Solids **17**, 117 (1960).
[6] R. C. Vickery, R. Sedlacek, and A. Ruben, J. Chem. Soc. **104**, 503 (1959).
[7] F. H. Spedding, K. Gschneider, Jr., and A. H. Daane, J. Am. Chem. Soc. **80**, 4499 (1958).

TABLE I. Crystallographic data.

REC_2	Lattice constants at 5°K (in Å)		Linear thermal expansion coefficients (in 10^{-6} deg^{-1})		Temperature factor coefficients, B (in Å^2)		Carbon positional parameters	C–C distances (in Å)	RE at (000)–C distances (in Å)	RE at $(\frac{1}{2}\frac{1}{2}\frac{1}{2})$–C distances (in Å)
	a	c	Parallel to a	Parallel to c	300°K	5°K				
CeC_2	3.875 ±0.001	6.477 ±0.003	3±1	6±2	0.60 ±0.04	0.40 ±0.05	0.4011 ±0.0005	1.281 ±0.007	2.598 ±0.003	2.814 ±0.001
PrC_2	3.852 ±0.001	6.425 ±0.002	3±2	5±2	0.98 ±0.14	0.64 ±0.11	0.3993 ±0.0005	1.294 ±0.006	2.566 ±0.003	2.800 ±0.001
NdC_2	3.820 ±0.001	6.390 ±0.002	3±1	8±2	0.52 ±0.10	0.34 ±0.08	0.3990 ±0.0007	1.291 ±0.009	2.550 ±0.004	2.777 ±0.002
TbC_2	3.678 ±0.001	6.206 ±0.001	11±2	6±3	0.67 ±0.06	0.30 ±0.05	0.3960 ±0.0007	1.291 ±0.009	2.458 ±0.004	2.680 ±0.002
HoC_2	3.633 ±0.002	6.132 ±0.002	9±2	4±2	0.88 ±0.02	0.35 ±0.10	0.3957 ±0.0007	1.279 ±0.009	2.426 ±0.004	2.647 ±0.003

and x-ray diffraction patterns, the spectroscopic and chemical analyses were carried out with emphasis on the residual RE metal and graphite, other RE–C compounds, and the high neutron-capturing impurities. The notable impurities were about 2 wt % of Ho_2C_3 in HoC_2, and the uncombined graphite ranged about 1.5% to 0.5% in all REC_2. Their small contributions have been subtracted from the neutron intensity data.

The powdered brassy yellow REC_2 samples, about 10 μ in average particle size, were mounted on the cryogenic instrument of an automatic multipurpose neutron diffractometer.[8,9] The diffraction patterns were then taken with the 1.069-Å neutrons at 300°–2°K.[10]

The low-temperature patterns exhibit extra reflections, all of which are assumed to be magnetic in their origin. No evidence contradicting this assumption has been found. The coherent nuclear-reflection analysis verified the x-ray results[7] that the chemical unit cell contains two molecules and possesses the body-centered-tetragonal symmetry, D_{4h}^{17}–$I4/m\ mm$. Our room-temperature lattice constants differ insignificantly from the literature values,[7] and those at 5°K are given in Table I. Also listed are the average linear thermal expansion coefficients in the temperature region, 5°–300°K. In the light REC_2, the expansion along the a axis is about a half of that along the c axis, while the relation is reversed in the heavy REC_2. Within our accuracy, no evidence of nontetragonal distortion was observed.

Table I summarizes other pertinent crystallographic data: the Debye–Waller temperature-factor coefficients, B in $\exp[-2B\ (\sin\theta/\lambda)^2]$, at 300° and 5°K; the carbon positional parameters, z in $(000, \frac{1}{2}\frac{1}{2}\frac{1}{2})\pm(00z)$, ($z=0$ for the RE atoms); the intramolecular C–C distances and the nearest C–RE distances at 5°K, with the statistical errors including the lattice-constant uncertainties but excluding the thermal vibration effect.[11] The coherent scattering amplitudes (b) employed are 0.662,[12] 0.482,[1] 0.44,[12] 0.72,[12] 0.76,[1] and 0.85,[12] all in 10^{-12} cm, for C, Ce, Pr, Nd, Tb, and Ho, respectively. The present data differ slightly from some of our previous values[1] on CeC_2 and TbC_2 at 300°K, but the differences are insignificant. In all cases, the B values decrease roughly linearly with the decreasing temperature. The Debye characteristic temperatures, Θ, computed from the B values using the average atomic mass, behave similarly and the TbC_2 case, as shown in Fig. 1, exemplifies these relations. The refined deduction[13] of Θ, which is inapplicable because of the lack of pertinent physical quantities, would not alter the above results substantially.

[8] M. Atoji, Nucl. Instr. Methods **35**, 13 (1965).

[9] M. Atoji, Argonne National Laboratory Rept. ANL-6920 (1964).

[10] The cold-finger specimen mount was employed (Ref. 9, pp. 76–81) using the following refrigerant: CCl_2F_2 for 243° to about 150°K, liquid N_2 for 77° to 63°K, solid N_2 for 63° to near 50°K, and liquid He for 4° to 2°K. The safety devices required for liquid H_2 in our CP-5 reactor are highly cumbersome and expensive, and hence liquid Ne (bp 27°K) was used instead. The neon gas (spark-chamber grade containing 10% He; Air Reduction Company) was precooled to 77°K and was slowly introduced into liquid He in the Dewar, thus producing solid Ne. The natural warming-up of the Dewar boils off the remaining liquid He and subsequently converts solid Ne to liquid Ne. Approximately ½ liter of liquid Ne (currently about $100) lasted about 40 h. In some experiments, a small measured amount of liquid N_2 is rapidly pumped out so as to form a known thickness of solid N_2 blanket over the cold finger. The Dewar is then filled with liquid He. Due to the heat insulation of solid N_2, the sample temperature range of 5° to about 30°K is attainable depending on the N_2-blanket thickness. However, the rate of liquid He vaporization increases considerably for thicker N_2 blanket. In our instrumentation (Ref. 9, p. 76), 1.5-in.-thick solid N_2 resulted in 20°K with the He vaporization rate of 1.2 liters/day, whereas without the N_2 blanket it is 0.35 liters/day. Also, the slow warming-up rate of the Dewar is frequently utilized, particularly in the Néel temperature determination. For warming the emptied inner chamber at 4.2°K to the outer-chamber temperature of 77°K, it takes about 10 to 24 h, longer for higher vacuum, depending on the amount of degassing in the vacuum chamber of the warming Dewar. When the temperature difference between the top and the bottom of the sample (Ref. 9, p. 76) was significantly large, the data were discarded. Our seemingly awkward temperature-variation technique could be substituted wholly by a variable-temperature Dewar such as the one with the helium-exchange gas scheme. However, the constant-temperature Dewar is still widely employed and our techniques described above should be of value in this aspect.

[11] W. R. Busing and H. A. Levy, Acta Cryst. **17**, 142 (1964).

[12] G. E. Bacon, *Neutron Diffraction* (Clarendon Press, Oxford, England, 1962), 2nd ed., p. 31.

[13] B. T. M. Willis, Proc. Roy. Soc. (London) **A274**, 134 (1963) and the references therein.

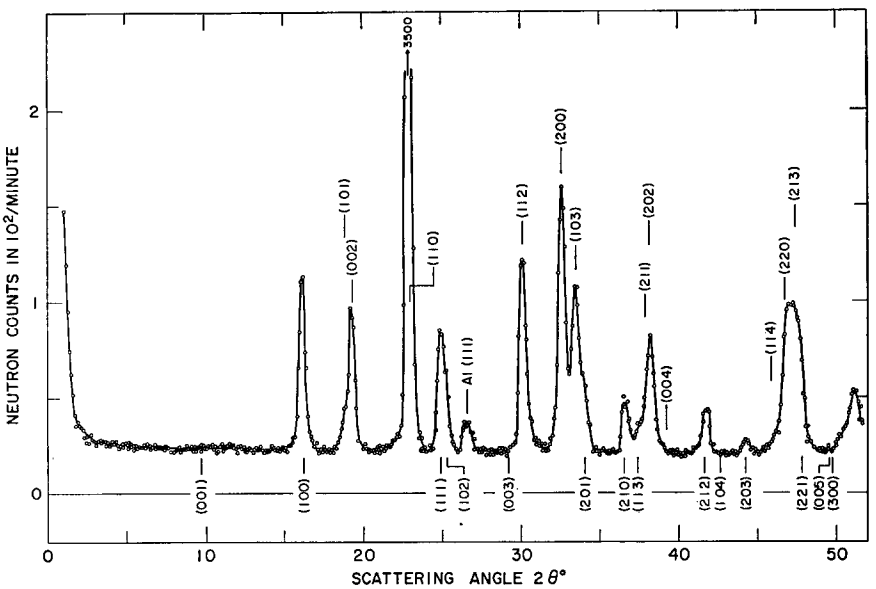

FIG. 2. The powder diffraction pattern of NdC_2 at 3°K. The indices for the nuclear and magnetic reflections are placed above and below the background, respectively. $\lambda = 1.069$ Å.

MAGNETIC STRUCTURES OF LIGHT REC_2

The paramagnetic diffuse backgrounds[14] of the light REC_2 at 300°K were reasonably interpretable using the free-ion Trammell form factors[4] with the effective nuclear charges for the $4f$ electrons, $Z-S=19$, 19, and 20 for Ce^{3+}, Pr^{3+}, and Nd^{3+}, respectively. In the vicinity of the liquid-He temperatures, there appeared additional peaks whose indices satisfy $h+k+l=2n+1$. The diffraction pattern of NdC_2 at 3°K is depicted in Fig. 2 as an example. These magnetic reflections represent a first-kind body-centered antiferromagnetic structure, i.e., the moment of RE at (000) is antiparallel to the moment at $(\frac{111}{222})$. The intensity analysis led to the moment direction that is parallel to the c axis.

The temperature dependency of the intensity of the strongest magnetic reflection, (100), was measured on the light REC_2 (Fig. 3). The Néel temperatures (T_N) thus obtained are 33°±2°, 15°±2°, and 29°±2°K for CeC_2, PrC_2, and NdC_2, respectively. The ordered moments of CeC_2, PrC_2, and NdC_2 are, respectively, 1.74±0.05, 1.14±0.05, and 2.95±0.05 Bohr magnetons (β) which are 81%, 44%, and 90% of the free-ion

[14] We assume in a first-order approximation that the diffraction background of our concern is the sum of the following scattering effects: (1) instrumental, (2) multiple, (3) nuclear incoherent, (4) elastic thermal diffuse, $\Sigma_j b_j^2\{1-\exp[-2B(\sin\theta/\lambda)^2]\}$, (5) (elastic paramagnetic)$\times(1-\alpha^2)$, where α is an order parameter, i.e., $\alpha^2=0$, when $T>>T_N$ and $\alpha^2=$(intensity of a given magnetic reflection at $T<T_N$)/(intensity of the same at the saturation temperature, T_s), (6) elastic magnetothermal diffuse,

$$\alpha^2(e^2\gamma/2mc)^2\Sigma g^2 J^2 f_m^2\{1-\exp[-2B(\sin\theta/\lambda)^2]\},$$

where the notations are explained in the text. We have excluded the strongly angular-dependent diffuse scattering, such as the thermal diffuse scattering usually associated with the Bragg–Laue peaks. As regards (1), the absorption and scattering modulation of the instrumental scattering due to the sample is difficult to evaluate in the case where the sample is surrounded by multiple enclosures as employed in the nonroom-temperature instrumentation. On the other hand, this correction can be applied straightforwardly in a single cylindrical-sample encasement as practiced in the room-temperature experiment (Ref. 9 pp. 44–46). Therefore, the room-temperature patterns of all REC_2 were taken without using the Dewar and the amount of (5) with $\alpha^2=0$ is then determined. Also, it was found that the multiple-scattering contribution is very much isotropic in all cases (see Ref. 1). In the 300°–4°K region, the instrumental scattering of the Dewar assembly with the emptied sample holder was unchanged except for the thermal effect on the Al-component peaks. Consequently, all sample background data at the sub-room temperatures are obtained from the difference patterns, taking the Dewar-mounted room-temperature data as a standard. We have assumed that the temperature dependency of the inelastic scattering from the sample is insignificantly small. Our neutron-sample packing was processed in pure, dry helium atmosphere so as to avoid the spurious scattering at low temperatures.

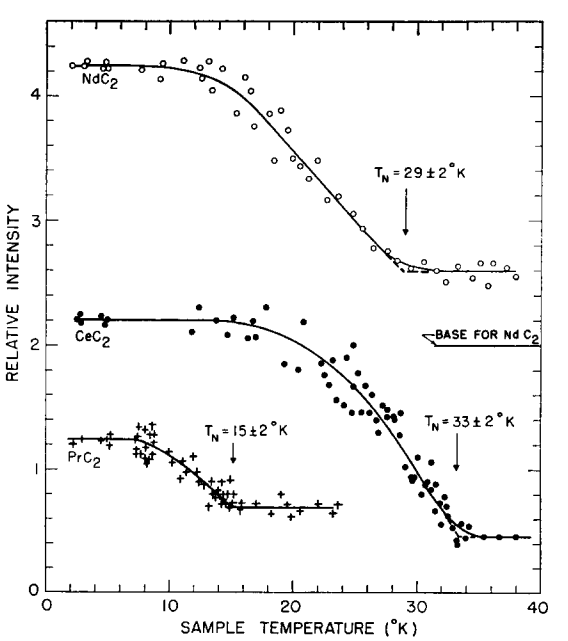

FIG. 3. The Néel temperature determination for the light REC_2 using the (100) magnetic reflection.

TABLE II. Observed and calculated intensities per unit cell in barns for the light REC_2 at 5°K. The magnetic reflections are designated by subscript m to the indices.

Indices	CeC_2		PrC_2		NdC_2	
	I_{calc}	I_{obs}	I_{calc}	I_{obs}	I_{calc}	I_{obs}
$(001)_m$	0	<2	0	<2	0	<2
$(100)_m$	82	80	53	54	240	236
101	217	342	238	335	72	235
002	121 (338)		99 (337)		176 (248)	
110	681	678	625	628	851	861
$(111)_m$	50	77	33	47	156	234
$(102)_m$	24 (74)		15 (48)		73 (229)	
$(003)_m$	0	<2	0	<2	0	<2
112	200	197	161	166	294	287
200	339	329	305	300	424	425
103	147	160	139	140	256	347
$(201)_m$	23 (170)		15 (154)		79 (335)	
$(210)_m$	21	18	14	15	71	74
$(113)_m$	7	244	5	230	26	248
211	109		115		36	
202	126 (254)		100 (234)		185 (252)	
004	12		14		5	
$(212)_m$	21	18	14	14	77	84
$(104)_m$	2	<2	1	<2	7 (84)	
$(203)_m$	6	7	4	4	23	21
114	34	364	41	323	14	515
220	168		146		212	
213	149 (359)		136 (328)		262 (519)	
$(221)_m$	8		5		31	
$(005)_m$	0	684	0	600	0	861
$(300)_m$	4		2		14	
301	31		32		10	
222	72		55		106	
204	27 (683)		32 (591)		12 (884)	
105	268		231		341	
310	267		229		339	
$(311)_m$	10		7		43	
$(302)_m$	4		3		19	
$(214)_m$	5	8	3	4	19	23
$(115)_m$	1 (6)		1 (4)		4 (23)	
$(223)_m$	3	126	2	92	14	204
312	118 (121)		89 (91)		176 (190)	
303	50	48	44	45	88	99

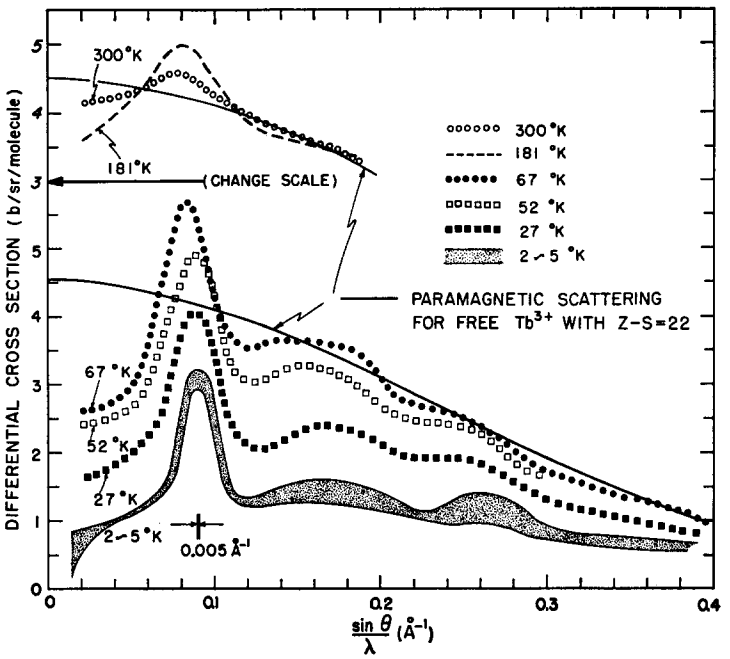

FIG. 4. The magnetic diffuse scattering of TbC_2 at representative temperatures. The shaded area implies the standard deviation which is also applicable to the 52°–27°K curves, while the errors of the curves for 300° to 67°K are about one-third of the shaded amount. The full width of the coherent peak near the highest hump is 0.005 $Å^{-1}$ in $\sin\theta/\lambda$ as illustrated in the figure.

values. No other magnetic transitions were found in the range, 300° to 2°K.

The preferred orientation effect was not detectable in the diffraction patterns. Although the magnetic peak profiles were normal, the small-angle scattering down to about 0.007 $Å^{-1}$ in $(\sin\theta)/\lambda$ was measured in each case to search for the satellite reflections associated with the origin of the reciprocal lattice. The result was negative. In the PrC_2 case, diffraction patterns were taken using samples of different particle sizes. Also, for seeking the impurity effect, the PrC_2 sample containing 1% Pr_2C_3, 0.5% Pr, and 2% graphite was subjected to the neutron experiment. Neither the particle size nor the impurity affects the magnetic data appreciably. The magnetic and nuclear intensity data at 5°K are compared with the calculated values in Table II.

MAGNETIC STRUCTURE OF TbC_2

The paramagnetic diffuse scattering of TbC_2 at 300°K shows a low, broad hump near $(\sin\theta)/\lambda=0.09$ $Å^{-1}$. The data at 250°, 181°, 79°, 77°, 69°, and 67°K show that, as the temperature is lowered, the hump steadily becomes higher and the smaller wavelets at higher angles become more noticeable (Fig. 4). The median or smoothened-out curve of the paramagnetic scattering at 300°K is consistent with our previous result that it is the free Tb^{3+} paramagnetic scattering with the effective nuclear charge for the $4f$ electrons, $Z-S=22$. The wavy modification of the paramagnetic scattering at 300°–67°K was interpretable based on the Slotnick formulas[15] for an antiferromagnetic short-range coupling between Tb at (000) and Tb at $(\frac{1}{2}\frac{1}{2}\frac{1}{2})$ with $-\mathcal{J}=0.40\pm0.07k$ in the exchange interaction, $-2\mathcal{J}J_iJ_j$. A better curve fitting can be attained by including other smaller, first-neighbor Tb–Tb interactions. However, their individual evaluation could not be made unambiguously, because of proximity in the interatomic distances. The crystal-field effect[4,5] in the paramagnetic TbC_2 is not as conspicuous as the HoC_2 case (cf. Figs. 4 and 8). Although less conclusive, the magnetic interaction mentioned above appears to be a partial ordering of the long-range-ordered magnetic structure which is described below.

The magnetic coherent peaks start to show up from the wavy background of the diffraction patterns at 65° and 64°K. The growth of these peaks becomes appreciable in the 57° and 52°K patterns, and Fig. 5 shows the difference pattern exhibiting only the coherent magnetic reflections at 52°K. These reflections were satisfactorily indexed on an enlarged cell, $a'=4a$, $b'=b$, and $c'=c$, where a, b, and c are the chemical unit-cell dimensions. The indices of the observed reflections in Fig. 5 satisfy the following relations: $h'=8n+1$ or $8n+7$, when $k+l=2n+1$; $h'=8n+3$ or $8n+5$, when $k+l=2n$. In the chemical reciprocal lattice, the magnetically diffracting lattice points are a pair of satellites having the indices, $(h\pm\frac{1}{4}, k, l)$, in which $h+k+l=2n+1$. We designate this structure as Type I. Actually, the indexing search for Type I was immediately fruitful through the use of the monographs for the modulus of the modulation vector vs $\sin\theta$, computed for various propagation directions of the modulation vector.[16] The detailed description of

[15] M. Slotnick, Phys. Rev. **83**, 1226 (1951).

[16] J. M. Hastings and L. M. Corliss, Phys. Rev. **126**, 556 (1962).

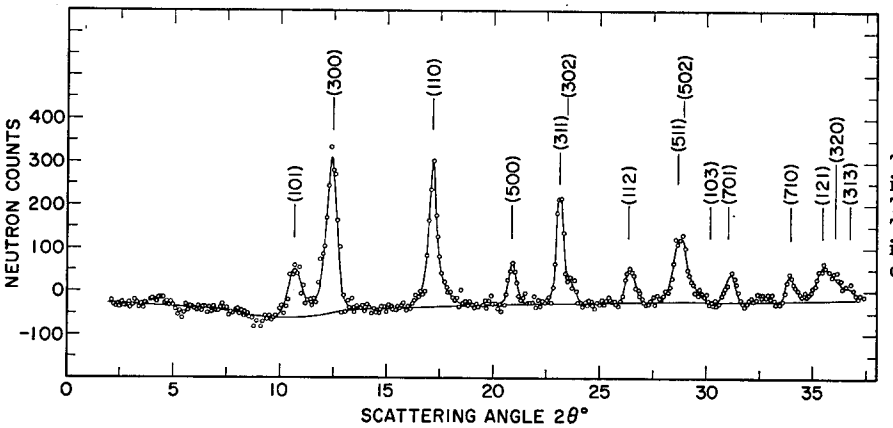

FIG. 5. The difference pattern for TbC_2 obtained by subtracting the intensity at 79°K from that at 52°K. The coherent peaks represent the Type I magnetic structure and their indices are based on the magnetic cell. $\lambda = 1.069$ Å.

this satellite-reflection parameter calculation and its computer program have been published elsewhere.[17]

The pattern at 27°K and those at the liquid-He temperatures show additional sets of magnetic reflections. Nevertheless, about 10 reflections of Type I are clearly resolvable in these patterns, and the intensity-temperature plotting for the representative reflections is given in Fig. 6, from which the Néel temperature for Type I is determined to be 66°±2°K.

For analyzing the Type I structure, we dissolve the ordered moment vector $g\mathbf{J}$ into three orthogonal components, i.e., $g\mathbf{J}=g\mathbf{J}_x+g\mathbf{J}_y+g\mathbf{J}_z$ with an implication of anisotropic "g". The satellitic indices, $h\pm\frac{1}{4}$, are interpretable as due to each moment component being sinusoidally modulated with the propagation direction along the a axis and with the successive phase-angle increment of 90° in the sinusoidal function. The anti-body-centered extinction associated with the magnetic satellites implies an antiferromagnetic coupling between the moments at the origin atoms and those at the body-centered positions. More quantitatively, the moment distribution is expressed by

$$\pm\left\{g\mathbf{J}_x\begin{matrix}\sin\\ \cos\end{matrix}\left(\frac{\pi}{2}\frac{x}{a}\right)+g\mathbf{J}_y\begin{matrix}\sin\\ \cos\end{matrix}\left(\frac{\pi}{2}\frac{x}{a}\right)+g\mathbf{J}_z\begin{matrix}\sin\\ \cos\end{matrix}\left(\frac{\pi}{2}\frac{x}{a}\right)\right\}. \quad (1)$$

Here, when the positive sign is given for the origin Tb atoms ($x=0$, a, $2a$, ··· etc.), the body-centered atoms ($x=\frac{1}{2}a$, $\frac{3}{2}a$, ··· etc.) take the negative sign.[18] Each moment component can choose either sine or cosine modulation independently. The least-squares treatments on various sine–cosine combinations[19] led to $g\mathbf{J}_x\cong 0$ and sine–cosine for $g\mathbf{J}_y$–$g\mathbf{J}_z$, for which the intensity expression per magnetic unit cell is given by

$$I_m = 16jf_m^2\left(\frac{e^2\gamma}{2mc^2}\right)^2\left[(1-e_y^2)(gJ_y)^2+(1-e_z^2)(gJ_z)^2\right]\times\frac{\exp[-2B(\sin\theta/\lambda)^2]}{\sin\theta\sin 2\theta}. \quad (2)$$

In this formula, j is the multiplicity factor for the orthorhombic system; f_m is the magnetic form factor obtained from the paramagnetic analysis; the unit scattering vector has been dissolved as $\mathbf{e}=\mathbf{e}_x+\mathbf{e}_y+\mathbf{e}_z$;

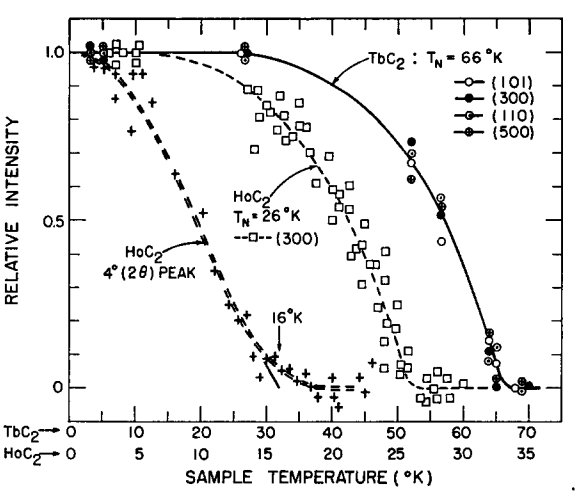

FIG. 6. The temperature dependency of the magnetic intensities in TbC_2 and HoC_2. The TbC_2 data are based on the integrated intensities and the HoC_2 data are obtained from the peak-height values.

[17] M. Atoji and J. Gvildys, Argonne National Laboratory Rept. ANL-7147 (1966).

[18] The phase angle difference between the x-axis moment component at the origin and that at the nearest body-centered position is 45° and the same is applied to the y and z components. The body-centered atom possesses the moment vector, (the vector sum of four nearest corner-atom moments)/$2\sqrt{2}$. In the magnetic unit cell, the sum of the squares of the moment components of the corner atoms is equal to the same sum for the body-centered moments.

[19] For instance, when we assign cosine, sine, and cosine to the x, y, and z modulations, respectively, one should add $(1-e_x^2)(gJ_x)^2-2e_ye_z(gJ_z)(gJ_x)$ to the moment sum term in Eq. (2). As regards the derivation of the intensity formula for the magnetic satellite reflection, see W. C. Koehler, Acta Cryst. **14**, 535 (1961); S. Hoshino and Y. Yamada, Buturi (Physics) **18**, 122 (1963); and Ref. 16.

the last multipliers are the temperature and Lorenz factors and other notations have their customary designations.

The final ordered-moment values are $gJ_x=0\pm0.3$, $gJ_y=1.6\pm0.3$, and $gJ_z=7.1\pm0.3\beta$ and the root-mean-square ordered moment per Tb is hence $5.1\pm0.2\beta$, which is also the moment at the body-centered position. The Type I magnetic structure of TbC_2 is illustrated in Fig. 7, and the observed and calculated magnetic intensities for Type I are listed in Table III.

As mentioned before, numerous additional coherent peaks crowd into the diffraction patterns at the lower temperatures. Some of these peak positions and their intensities are different in 27° and 5°–2°K patterns. We call this lower-temperature structure Type II. A number of trial models based on the reasonably enlargened unit cells as well as various sinusoidal and antiphase domain structures have failed to characterize the Type II magnetization. The single-crystal data seem inevitably needed here. The temperature

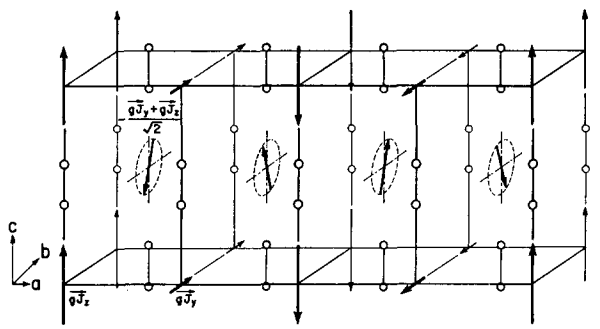

FIG. 7. Schematic representation of the Type I antiferromagnetic structure found in TbC_2 with $T_N=66$°K and also in HoC_2 ($gJ_y=0$) with $T_N=26$°K. The small circles represent the C_2 molecules and the moment vectors are placed at the metal-atom positions.

dependencies of several representative reflections indicate that the Type II magnetic transition takes place at 35°–30°K, except for a peak at 4° in 2θ which starts to appear at $40°\pm5$°K. The $4°(2\theta)$ peak intensity corrected for a large Lorenz factor is very small and no other peaks having the same thermal magnetization were found. Now, $4°(2\theta)$ is the scattering angle of the (100) magnetic reflection which is the Type I satellite associated with the origin of the reciprocal lattice. If this peak is due to a deviation from the antiferromagnetic balance in the Type I structure, the maximum possible unbalanced moment at 2°K is $0.54\pm0.03\beta$, which is too small to give rise to the appreciably strong reflections at the higher angles.

As illustrated in Fig. 4, the magnetic coherent peaks develop at the expense of lowering the magnetic diffuse background. In spite of this, the main features of the background waviness remain essentially the same and this persists down to near 2°K. If the forward scattering cross section deduced from the median diffuse

TABLE III. The observed and calculated intensities per Tb [Eq. (2) divided by 64] in barns for the Type I magnetic structure of TbC_2 at 5°K. The indices are given in terms of the magnetic unit cell.

Indices	I_{calc}	I_{obs}
101	40	40
300	74	70
110	69	60
500	22	23
311	55	57
302	11	15
112	21	18
511	33	55
502	10	
	43	
103	1	~0
701	13	13
710	11	11

background is related to $\mu_{eff}=g[J(J+1)]^{1/2}$ in a manner similar to the paramagnetic analysis, the observed data follow roughly $\mu_{eff}^2=36+0.89T$ in β^2. This may imply that a sizable amount of fluctuating moments with a short-range order coexists with the long-range ordered moments.[20] Other probable, alternative models which can also generate the observed humps are an antiphase domain structure with variant periodicities and a retarded spiral model of HoN type.[21] The diffuse scattering data at the temperatures

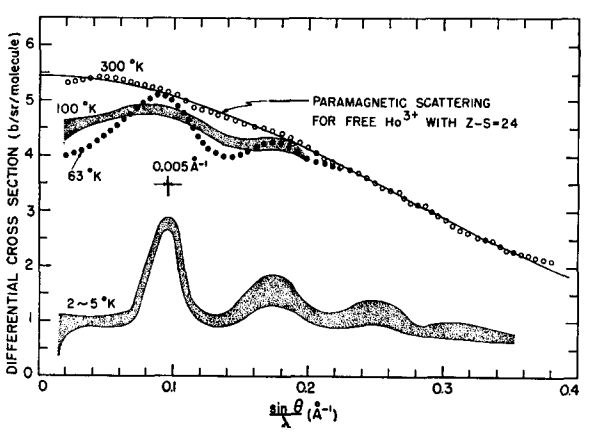

FIG. 8. The magnetic diffuse scattering of HoC_2 at representative temperatures. The standard deviation implied by the shaded area for the 2°–5°K curve is applicable to the 100° and 63°K curves, while the 300°K curve has about threefold higher accuracy. The full-width at half-height of the coherent peak, 0.005 $Å^{-1}$, is also indicated.

[20] G. T. Trammell, Phys. Rev. **131**, 932 (1963).
[21] H. R. Child, M. K. Wilkinson, J. W. Cable, W. C. Koehler, and E. O. Wollan, Phys. Rev. **131**, 922 (1963).

TABLE IV. Observed and calculated intensities (in barns) per HoC_2 at 5°K. The magnetic indices are designated by subscript m and are based on the magnetic unit cell. The nuclear reflections are indexed on the chemical unit cell.

Indices	I_{calc}	I_{obs}	Indices	I_{calc}	I_{obs}
$(101)_m$	55	52	$(513)_m$	11	11
$(300)_m$	131	129	$(322)_m$	17	
$(110)_m$	129	131	$(910)_m$	11	
101	5		$(304)_m$	1	34
002	47	52	$(703)_m$	5	
$(500)_m$	41	51	$(114)_m$	3	~3
$(311)_m$	103		$(522)_m$	13	13
$(302)_m$	17	115	$(504)_m$	2	
110	218	227	$(123)_m$	9	
$(112)_m$	39	41	$(721)_m$	14	
$(511)_m$	63		$(912)_m$	12	44
$(502)_m$	18	88	$(11, 0, 0)_m$	4	
$(103)_m$	1	<2	114	2	
112	77		220	54	
$(701)_m$	25	98	213	83	130
200	108		$(903)_m$	4	
$(710)_m$	22	218	$(105)_m$	0	
103	82		$(11, 1, 1)_m$	9	
$(121)_m$	35		$(11, 0, 2)_m$	4	20
$(320)_m$	18	66	$(130)_m$	5	
$(313)_m$	11				
211	3				
202	48				
$(901)_m$	13				
$(712)_m$	20	97			
$(520)_m$	13				
004	1				

near 66°K suggest that the critical scattering associated with the Type I structure is significant only at $(\sin\theta)/\lambda<0.02$ Å^{-1}, where our experimental error is considerably large.

MAGNETIC STRUCTURE OF HOC_2

As shown in Fig. 8, the paramagnetic diffuse scattering of HoC_2 is similar to the TbC_2 case (cf. Fig. 4). When a slight waviness observed in the paramagnetic scattering curve at 300°K is averaged out, it is closely approximated by the free-ion Trammell form factor with $Z-S=24$ rather than 21 reported for Ho_2O_3. The wavy nature of the paramagnetic curves observed at 300°, 100°, 79°, 70°, and 63°K is roughly accounted for by an antiferromagnetic short-range order between the origin Ho atom and the body-centered Ho atom with $-\mathcal{J}=0.1$–$0.2k$ being considerably smaller than the corresponding value in TbC_2. In HoC_2, the median levels of the scattering curves at low angles are notably suppressed from the free-ion level (Fig. 8). This is apparently due to the crystal-field effect which is not noticeable in TbC_2 at $T>66$°K.

The diffraction pattern at 5°K is shown in Fig. 9, in which the nonnuclear reflections excluding the reflection at 4° in 2θ were successfully interpreted as due to the Type I magnetic structure. The temperature

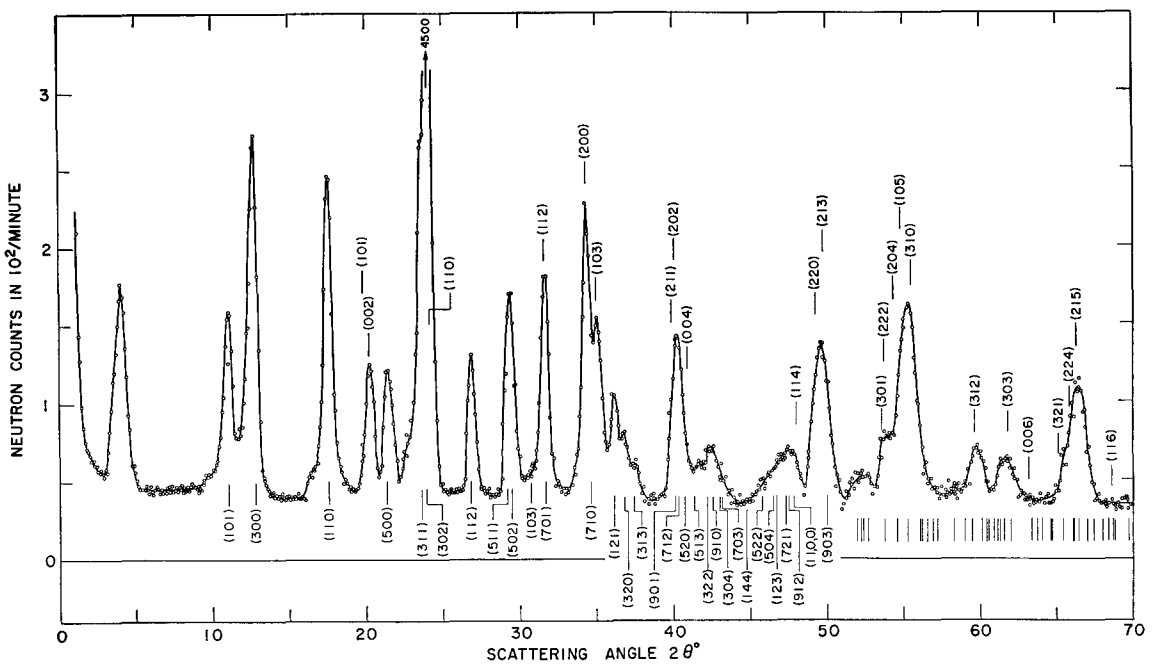

FIG. 9. The powder diffraction pattern of HoC_2 at 5°K. The indices for the nuclear reflections are shown above the diffraction curve and the magnetic indices based on the magnetic unit cell are given in the background. $\lambda = 1.069$ Å.

dependency of the peak intensity of the (300) reflection is given in Fig. 6, from which the Néel temperature for the Type I structure was determined as 26°±2°K. The least-squares treatment led to the ordered moment values, $gJ_x = 0 \pm 0.5$, $gJ_y = 0 \pm 0.5$, and $gJ_z = 9.75 \pm 0.05\beta$. The root-mean-square moment per Ho atom is therefore $6.89 \pm 0.04\beta$. The diffraction data at 2°K gave the same value and show no evidence of the Type II magnetic phase. The observed and calculated intensities at 5°K for both the nuclear and Type I magnetic structures are listed in Table IV.

The temperature dependency of the peak height of the 4°(2θ) reflection is shown in Fig. 6, which gives the transition temperature of about 16°K. If one assumes that this reflection is due to a ferrimagnetic modulation of the Type I structure as postulated in the TbC_2 case, the maximum possible unbalanced moment at 2°K is $1.65 \pm 0.08\beta$ per Ho atom which is about threefold the corresponding moment in TbC_2. If the moment at the origin atom retains 9.75β, then

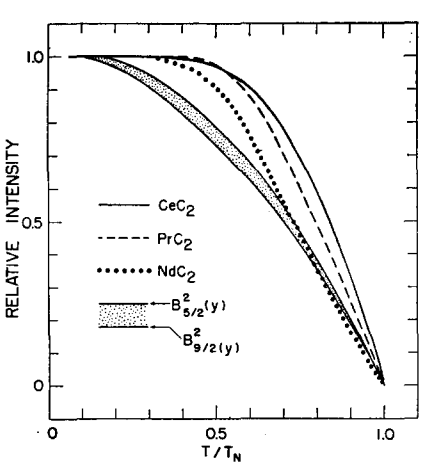

FIG. 10. The normalized thermal magnetization curves of the light REC_2. The estimated maximum experimental errors are about 10% for CeC_2 and NdC_2, and 15% for PrC_2. The Brillouin values for the free ions lie within the shaded area. The PrC_2 curve approximates closely the Brillouin curve for $S = \frac{1}{2}$.

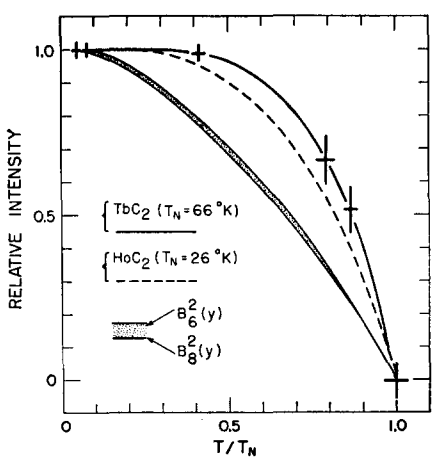

FIG. 11. The normalized thermal magnetization curves for the Type I magnetic structure of TbC_2 and that of HoC_2. The estimated maximum errors indicated by the cross figures for TbC_2 are also applicable to HoC_2 except for doubling the errors in the temperature scale. The Brillouin curves for the free ions are shown for comparison. The HoC_2 curve follows approximately the Brillouin curve for $S = \frac{1}{2}$.

the maximum possible moment at the body-centered position becomes $6.89+1.65=8.54(\pm 0.09)$ in β. Hence, the maximum possible root-mean-square moment per Ho atom at 2°K is $\{[(9.75)^2(2)+(8.54)^2(4)]/8\}^{1/2}=7.76\beta$, while the free ion gives $gJ=10.0\beta$.

The magnetic diffuse background at $T<26$°K is quite analogous to the TbC_2 data. The forward cross-section values led to $\mu_{eff}^2=22+2.7T$ (maximum error, 25%) in β^2 at $5°<T<26$°K, but this interpretation is far from unique. The highest hump in Fig. 9 lies underneath the magnetic reflections, (101) and (300). When the no-hump background is assumed there ignoring the resultant irregular peak profiles of these two magnetic reflections, an imaginary moment value, $gJ_x=3i\beta$, was obtained, thus disapproving such interpretation.

DISCUSSION

As regards the crystal structures, it is very likely that REC_2 has only two crystallographic modifications, a cubic form existing near the melting point as found in LaC_2 above 1750°C[22] and the tetragonal CaC_2-type structure stable down to near 0°K. On the other hand, two additional modifications are known for CaC_2 above 77°K.[23] As regards the thermal-expansion coefficients, our data (Table I) may imply that in the light REC_2 the magnetic-dipole repulsion along the c axis is larger than that along the a axis and the relation is reversed in the heavy REC_2.

The magnetic form factors obtained from the high-temperature paramagnetic scattering analyses are closely represented by the Trammell form factors using the hydrogenlike wavefunction[4] with the effective nuclear charge as a fitting variable. On the other hand, the Trammell form factors with the Hartree–Fock wavefunctions[24] are consistently larger than the observed form factors in all REC_2 compounds, and the differences are larger at higher angles. In the Tb case, for instance, the percentage discrepancies in f_m^2 are as much as 16%, 33%, and 56% at $(\sin\theta)/\lambda=0.35$, 0.4, and 0.5 Å^{-1}, respectively. This aspect has also been pointed out by Blume *et al.*[24] in citing the Oak Ridge form factors for Nd^{3+}, Ho^{3+}, and Er^{3+}, but no satisfactory explanation is known as yet.

The normalized magnetization curves of the light REC_2 are given in Fig. 10 and those for the heavy-REC_2 Type I structures are shown in Fig. 11. In all cases, the observed data are significantly different from the free-ion Brillouin curves, but follow rather closely the Brillouin curves for $S=\frac{1}{2}$ or nearby S values or an admixture of these low S values. Although the experimental errors are large, this suggests a complex magnetic-energy-level configuration that also accounts for the observed ordered moments. The temperature dependency of the $4°(2\theta)$ peak intensity of HoC_2 (Fig. 6) is approximated by the free-ion Brillouin curve, but the agreement here is probably accidental.

The observed ordered moments in the light REC_2 are significantly smaller than the free-ion values and this is very likely due to the crystal-field splittings counteracting on the exchange couplings. If the crystal-field splittings are larger than the exchange forces (and therefore larger than kT), one expects a smaller ordered moment for an even number of $4f$ electrons than for an odd-number case. This is just what we observed in the light REC_2 series. G. Goodman of our Division pointed out that if our tetragonal field is represented by a large cubic term with smaller tetragonal terms, the cubic field should be closer to that for the cube coordination than for the octahedral configuration.[25] The ground states in concern are hence probably Γ_8, Γ_1 and/or Γ_5, and Γ_8 (Bethe's notations) for Ce, Pr, and Nd, respectively. A similarity between the magnetic properties of CeC_2 and NdC_2 is then understandable, and a small ordered moment of PrC_2 may suggest an appreciable contribution of the non-magnetic Γ_1 state.

The crystal-field effect is also apparent in HoC_2 as demonstrated by the paramagnetic scattering and also by the ordered moment. The differences in the magnetic-structure data of TbC_2 and HoC_2 may be caused by the complex, dissimilar, crystal-field splittings which are comparative or smaller than the exchange forces. The Type I spin alignments found in TbC_2 and HoC_2 may be termed as anisotropic or elliptic helices whose propagation periods are commensurable with the chemical lattice repetition. No such structure has previously been reported. It should be noted that the helix propagation is along the shortest metal–metal distance, which is only several percent longer than the neighboring metal–metal distances in the RE metal. Another striking feature in the observed Type I structures is that every other RE atom in the origin row along the a axis generates a small ordered moment or none at all. The wavy magnetic diffuse scattering at the magnetically ordered temperatures in the heavy REC_2 is also puzzling, although Trammell has given a brief account on this subject.[20] A similar diffuse background was observed in PrC_2 at the ordered temperatures. Unfortunately, reliable physical quantities on REC_2 are still scarce,[26] and this has hampered further elucidation of the subject matter.

Since the indirect exchange interaction of the $4f$ electrons via the conduction electrons is a determinant factor in the long-range cooperative alignment of the

[22] M. A. Bredig, J. Am. Ceram. Soc. **43**, 493 (1960).
[23] N. G. Vannerberg, Acta Chem. Scand. **16**, 1212 (1962), and references therein.
[24] M. Blume, A. J. Freeman, and R. E. Watson, J. Chem. Phys. **37**, 1245 (1962).
[25] K. R. Lea, M. J. M. Leask, and W. P. Wolf, J. Phys. Chem. Solids **23**, 1381 (1962).
[26] K. A. Gschneider, Jr., *Rare Earth Alloys* (D. Van Nostrand Co., Inc., Princeton, N.J., 1961), pp. 138–140.

$4f$ local moments,[27] we look into the probable conduction-band scheme for REC_2. The electronic structure of REC_2 has been postulated as RE^{3+} plus C_2^{2-} plus one conduction electron.[1-3] These conduction electrons occupy the delocalized energy band originated from the $5d$ orbitals of RE and the antibonding orbitals ($\pi_g 2p$) of the C_2 molecule. This model explains the metallic character, a long C–C distance, and the zero Knight-shift value found in YC_2,[28] although the Hall coefficient leading to the number of the conduction electrons is not known. The wavefunctions pertinent to our model are depicted in Fig. 12, where the molecular orbital parameters of C_2 are those employed by Clementi and Pitzer[29] and the Slater functions are used for the RE atom. Here, it should be noted that among the available orbitals, the Knight-shift result and the site symmetries allow the combinations, $\pi_g 2p$ to $5d_{zx}$ and to $5d_{yz}$ ($z \equiv c$ axis), as the most probable constituents of the conduction band. The periodic potential for the conduction electron in REC_2 is hence due presumably to an alternating array of the positive RE^{3+} and the negative C_2^{2-} cores, in contrast to the positive-only cores in the usual metal. An inverted conduction-band theory[30] may be applicable to REC_2. Ern and Switendick[31] have given an extensive theory on the band structure of TiC, but the C_2 group[29] should possess a much larger electronegativity than C in TiC. The crystal structure of $MnAu_2$ is isomorphous to REC_2. However, the Au atoms in $MnAu_2$ form a staggered c layer rather than the Au_2 groups. The magnetic spin alignment in $MnAu_2$ is well known[32] and its helical structure is entirely different from the Type I structure. These considerations emphasize further the uniqueness of the magnetic properties of REC_2.

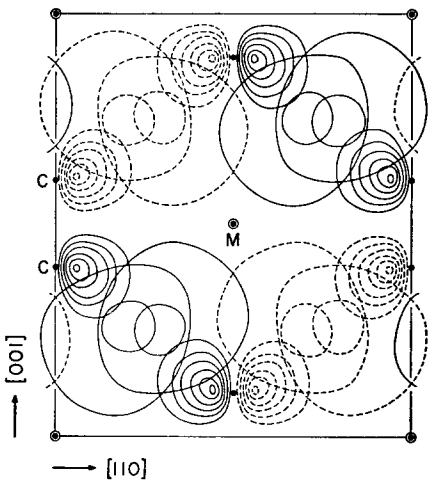

FIG. 12. The (110)-zone section of the normalized wavefunctions, $\pi_g 2p$ of the C_2 molecule and $5d_{zz}$ of the RE atom in REC_2, where the x axis of the d_{zz} is taken parallel to the [110] axis. Each contour line represents an increment of 0.5 [electrons/(Bohr radius)^3]$^{1/2}$, the lowest contour line being equal to unity. The negative values are indicated by broken lines.

ACKNOWLEDGMENTS

The author is greatly indebted to Dr. F. H. Spedding and Dr. A. H. Daane for providing the samples of CeC_2 and TbC_2, to Dr. J. L. Moriarty for preparation of PrC_2 and NdC_2, and to Mr. J. Gvildys for his help in the computer data processing.

[27] R. E. Watson, S. Koide, M. Peter, and A. J. Freeman, Phys. Rev. **139**, A167 (1965).
[28] R. G. Barnes (private communication).
[29] E. Clementi and K. S. Pitzer, J. Chem. Phys. **32**, 656 (1960).
[30] J. M. Keller, J. Chem. Phys. **33**, 232 (1960).
[31] V. Ern and A. C. Switendick, Phys. Rev. **137**, A1927 (1965).
[32] A. Herpin, P. Meriel, and J. Villain, Compt. Rend. (Paris) **249**, 1334 (1959).